



MAX-PLANCK-GESELLSCHAFT

## BACHELOR'S THESIS

# Impact of variations in the density profile on the bootstrap current in a tokamak edge plasma

zur Erlangung des akademischen Grades

**Bachelor of Science (BSc)**

im Rahmen des Studiums

**Technische Physik**

eingereicht von

**Samuel Lechner**

Matrikelnummer 12007552

ausgeführt am Institut für Angewandte Physik der Technischen Universität in Wien  
in Zusammenarbeit mit dem Max-Planck-Institut für Plasmaphysik

Betreuung:

Univ.Prof. Mag.rer.nat. Dipl.-Ing. Dr.techn. Friedrich Aumayr

Univ.Prof.in Dipl.-Ing.in Dr.in techn. Elisabeth Wolfrum

Projektass.in Dipl.-Ing.in. Lidija Radovanovic BSc

Wien, 13.12.2023

---

Samuel Lechner

---

Friedrich Aumayr

# Contents

<b>1</b>	<b>Introduction</b>	<b>5</b>
1.1	Conventional Energy Generation . . . . .	5
1.2	Nuclear Fusion . . . . .	6
1.3	Magnetic Confinement . . . . .	7
1.4	ASDEX Upgrade . . . . .	8
1.5	Transport in a Tokamak . . . . .	9
1.6	Aim of this thesis . . . . .	9
<b>2</b>	<b>Tokamak physics</b>	<b>10</b>
2.1	Geometry . . . . .	10
2.2	Magnetic Fields . . . . .	10
2.3	Heating and Fueling . . . . .	11
2.4	Diagnostics and IDA . . . . .	12
2.5	Equilibrium . . . . .	12
2.5.1	Equations . . . . .	12
2.5.2	Magnetic Flux Surfaces . . . . .	13
2.5.3	Density, Temperature and Pressure . . . . .	13
2.5.4	Instabilities . . . . .	14
2.6	Collisionality . . . . .	15
2.7	Transport . . . . .	15
2.7.1	Trapped free Particles . . . . .	15
2.7.2	Banana Currents . . . . .	16
<b>3</b>	<b>Bootstrap Current</b>	<b>18</b>
3.1	Computational Methods . . . . .	18
3.2	Collisions between Trapped and Passing Particles . . . . .	18
3.3	Accuracy Evaluation and Further Improvement . . . . .	21
3.4	Comparison with other Models . . . . .	21
3.4.1	Sauter Model . . . . .	21
3.4.2	NEO . . . . .	22
3.4.3	Integrating NEO with the Sauter Model . . . . .	22
<b>4</b>	<b>Manipulation of Density Profiles</b>	<b>23</b>
4.1	Original Density Profile . . . . .	23
4.2	Manipulation methods . . . . .	23
4.2.1	Constant Horizontal Shift . . . . .	25
4.2.2	Constant Vertical Shift . . . . .	26
4.2.3	Pedestal's Height Shift . . . . .	27
4.2.4	Pedestal Steepness Shift . . . . .	28
<b>5</b>	<b>Impact on the Bootstrap Current</b>	<b>29</b>
5.1	Original Bootstrap Current Profile . . . . .	29
5.2	Determination of the Bootstrap Current using manipulated Density Pro- files . . . . .	29
5.2.1	Using Constant Horizontal Shift Manipulation . . . . .	30
5.2.2	Using Constant Vertical Shift Manipulation . . . . .	31
5.2.3	Using Pedestal's Height Shift Manipulation . . . . .	32

5.2.4	Using Pedestal's Steepness Shift Manipulation . . . . .	33
<b>6</b>	<b>Summary and Results</b>	<b>34</b>
<b>A</b>	<b>Appendix</b>	<b>36</b>
A.1	Source Code . . . . .	36

## **Abstract**

This thesis delves into the intricate realm of nuclear fusion, focusing on the dynamic operational mechanisms of doughnut-shaped tokamak fusion reactors employing magnetic confinement to sustain plasma. Within these reactors, a nuanced examination unfolds, differentiating between classical, neoclassical, and turbulent transport phenomena. The neoclassical transport characterizes the movement of particles in a plasma by considering both collisions and the influence of non-uniform magnetic fields arising from the toroidal geometry.

The Bootstrap current arises as a direct consequence stemming from neoclassical transport theory. It is an electric current self-generated within the plasma due to radial gradients in temperature and density and flows parallel to magnetic field lines, significantly contributing to the overall current density in the system. It profoundly influences magnetohydrodynamics in the pedestal region, but its understanding is complex due to its dependence on multiple intertwined factors, posing a challenging task in isolating individual impacts.

In a tokamak, plasma confinement primarily relies on a magnetic field generated by a toroidal electric field, originating from the flux change in a central coil, in which the current strength is continually changed. Consequently, this method renders fusion a pulsed process due to limitations in sustaining this magnetic configuration over time. Maintaining the tokamak in a steady state becomes crucial, and the bootstrap current plays a pivotal role in supporting this stability. However, the primary focus of this thesis lies elsewhere.

This thesis examines the specific influence of density profile variations on the Bootstrap current. To explore this, diverse modified density profiles are systematically generated and compared. These profiles are subsequently employed in computing the Bootstrap current using an approximation method, alongside the original density profiles. Furthermore, the impact of these variations on collisionality are elucidated.

The analysis in this bachelor thesis reveals that altering the density profile has diverse and occasionally counterintuitive effects on the Bootstrap current. This complexity arises from the distinct impacts of both density and its gradient on the current in combination with the temperature. In addition, the approach of manipulating density profiles could prove intriguing in various other scenarios where the isolated effect of density is under scrutiny.

# 1 Introduction

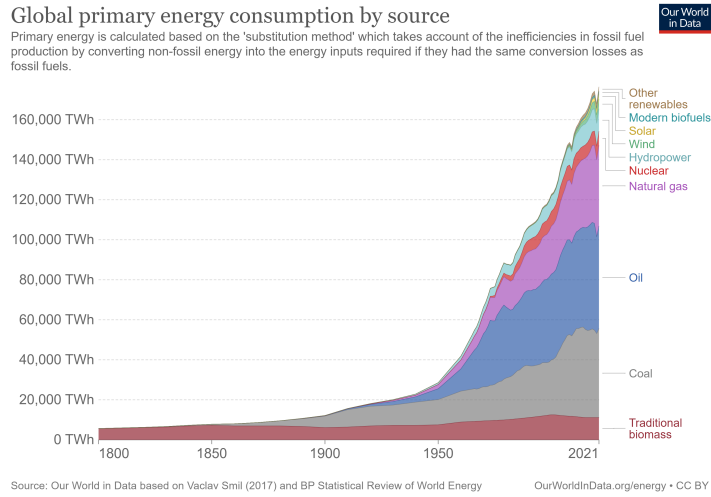


Figure 1: Global primary energy consumption by source  
(figure taken from [1])

## 1.1 Conventional Energy Generation

Since the beginning of the industrial revolution in the 18th century, the worldwide demand for energy has constantly increased to more than 175 TWh in 2021 [1]. Until today most of the electricity has been generated by burning fossil fuels like coal, oil or gas. Figure 1 shows the development of energy generation since 1800. However, there are many issues that come along with fossil fuel combustion such as:

- Fossil fuels combustion leads inevitably to a rise of carbon dioxide in the earth's atmosphere and amplifies the green house effect. Therefore, earth's average temperature on the surface has risen dramatically since pre-industrial times. It has been widely proven that there is a linear correlation between CO<sub>2</sub> concentration in the atmosphere and the average atmospheric temperature [2].
- Furthermore, in the processes of fossil fuel combustion, a range of other harmful air pollutants such as nitrogen oxides, sulfur dioxide, and particulate matter are released. This can lead to respiratory and cardiovascular problems, exacerbate asthma and other respiratory illnesses, and increase the risk of premature death. [3]
- Moreover, fossil fuel combustion is not sustainable in the long term due to the finite nature of fossil fuel resources. Continued reliance on these non-renewable resources will eventually lead to energy scarcity, making it imperative to transition towards sustainable energy sources. [4]

In the mid of the 20th century the first commercial nuclear fission power plants were established. Nuclear power has a fundamental advantage compared to fossil fuel power. Whilst combustion is a chemical process that takes place outside the atomic

nucleus in the electron shells, both nuclear fission and fusion takes place inside the atomic nucleus by overcoming weak interaction forces. Generating electricity with nuclear fission power was a lot better than burning fossil fuels with regard to economy, efficiency, environmental impact and many more.

The Chernobyl disaster of 1986, caused by human error, had a profound impact on public perception of nuclear energy, raising serious concerns about their safety and sustainability. However, it's worth noting that the safety aspects of nuclear fusion is quite different from those of fission. Nevertheless, the question how to dispose nuclear waste from fission safely and without causing long-term damage to the environment remains unanswered. Despite these concerns, the European Union recently labeled both nuclear energy and gas as sustainable energy resources, leading to widespread criticism [5].

In recent years, conventional renewable energy sources such as solar and wind power have become increasingly popular. However, nuclear fusion is a highly promising source of clean energy that offers safety and efficiency benefits. Unlike solar and wind power, which are dependent on specific weather conditions, fusion power plants have the potential to generate a consistent and reliable supply of energy to meet the basic demand load. Moreover, fusion power plants require less space than wind or solar parks to generate the same amount of power and can be constructed regardless of regional conditions.

However, there are currently no economically viable fusion reactors due to a lack of technical and engineering expertise.

## 1.2 Nuclear Fusion

Nuclear fusion is the process that powers the stars. In the Sun, the most common fusion reaction is the one between two hydrogen ions, even though this reaction is not the most efficient one. Due to the large mass of the stars, in these conditions it is still feasible.

However, when trying to achieve nuclear fusion on earth, it is more suitable to use the nuclear reaction between two hydrogen isotopes: deuterium and tritium. Both can be obtained in almost unlimited quantities from the Earth's oceans. This reaction fortunately takes place under less temperature and pressure. The resulting products are an  $\alpha$ -particle (helium-4 nucleus) used for heating and a high-energy neutron that can be harnessed to produce electricity. Figure 2 illustrates the process wherein deuterium and tritium fuse to form an  $\alpha$ -particle and a neutron.

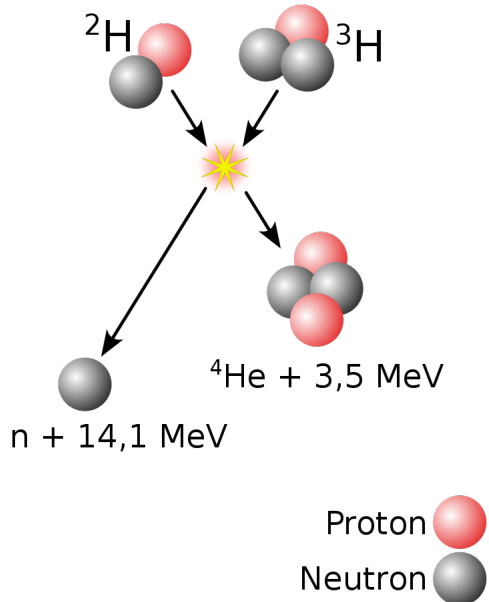
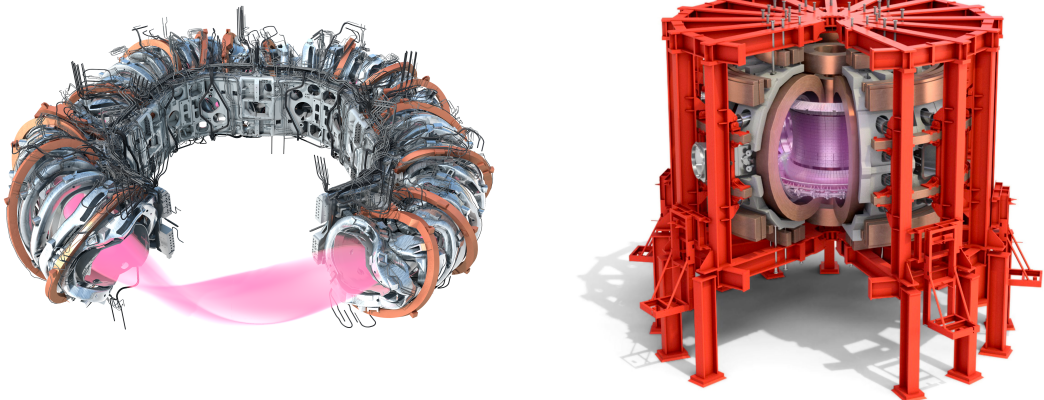


Figure 2: Fusion process on earth:  
 When deuterium (upper left) and tritium (upper right) undergo fusion, they produce an  $\alpha$ -particle and a high-energy neutron.  
 (figure taken from [6])

### 1.3 Magnetic Confinement

The process of fusion occurs within a plasma, a quasineutral gas of charged and neutral particles, but it can only be achieved and sustained if the plasma is properly confined. There are typically two approaches to accomplishing this confinement. Inertial confinement on the one hand uses laser beams to heat up the surface of a fuel pellet evenly until the density of the fuel is high enough to enable fusion.

Magnetic confinement, on the other hand uses both toroidal and poloidal magnetic fields to keep the plasma in its place. Essentially there have been established two types of fusion reactors both using magnetic confinement but that differ in their fundamental design: As examples, figure 3a shows the stellarator W7-X, and 3b the tokamak ASDEX Upgrade. Both of them use magnetic devices for providing the toroidal magnetic fields. However, with respect to the poloidal magnetic fields, while the stellarator only makes use of magnetic devices, the tokamak, in addition to that, utilizes an electrical current that flows in torus direction and also generates magnetic fields by itself. [7]



(a) Stellarator: Wendelstein 7-X  
in Greifswald, Germany  
(figure taken from [8])

(b) Tokamak: ASDEX Upgrade  
in Garching, Germany  
(figure taken from [9])

Figure 3: Two different types of fusion reactors both run by the *Max-Planck-Institut für Plasmaphysik*

## 1.4 ASDEX Upgrade

The fusion reactor from which the data used in this paper come from is **ASDEX Upgrade**, a tokamak fusion reactor run by *Max-Planck-Institut Für Plasmaphysik* (IPP) since 1991. Its plasma ring has a radius of 1.65 metre, a volume of 13 cubic metres and a total weight of about 800 tons. The inner wall of the centered steel vessel is clad with tiles made of tungsten metal. ASDEX Upgrade's 40 diagnostics are capable of recording up to 4 gigabyte of raw data per discharge whose results are partly available within less than milliseconds for feedback control and further data analysis. Figure 4 shows the vessel and the inner wall of ASDEX Upgrade.[10]



Figure 4: Plasma vessel of ASDEX Upgrade  
(figure taken from [11])

## **1.5 Transport in a Tokamak**

In a tokamak, various types of transport mechanisms are present. Turbulent transport prevails in the plasma core, characterized by high density and temperature. In H-mode (high confinement mode), an operational regime where a certain heating threshold is exceeded and the energy confinement time is increased by a factor of 2 with respect to the so-called L-mode (low confinement mode), a transport barrier called the pedestal causes a sudden reduction in plasma pressure. Consequently, while turbulent transport diminishes in significance, neo-classical transport becomes prominent within this pedestal region. [7]

Neo-classical transport primarily arises from particle collisions, which significantly influence the Bootstrap current. Detailed insights into collisionality and the Bootstrap current will be provided in chapter 2 and 3.

## **1.6 Aim of this thesis**

The Bootstrap current is a self-generated current that is highly valuable in tokamak machines. It arises due to both tokamak curvature and gradients in the toroidal magnetic field and is primarily influenced by pressure gradients. Given that it is obtained without any additional input, optimizing its utilization is crucial for efficient operation.

However, pressure- and current gradients are strongly entangled, particularly in the pedestal region. To break this connection and investigate the effect of each gradient on its own, one can artificially manipulate one of them, such as density, and observe changes in the other.

This thesis aims to study the impact of such changes on the Bootstrap current and the collisionality, which has significant practical relevance in processes where the density profile changes, such as during heating and fueling events.

## 2 Tokamak physics

In order to understand the motivation behind further investigations on the bootstrap current it's worth having a closer look on how a tokamak reactor works in general.

### 2.1 Geometry

In simple terms a tokamak is a doughnut-shaped tube. To describe certain points of the tokamak there can be introduced toroidal ( $Z, R, \Phi$ ) and poloidal ( $r, \Theta$ ) coordinates. Two typical quantities of a tokamak are the major plasma radius  $R_o$  and the minor plasma radius  $r_o$ . Hence, the *aspect ratio* can be defined as  $R_o/r_o$  and consequently the inverse aspect ratio  $\epsilon$  as  $r_o/R_o$ . Figure 5 shows the toroidal and poloidal coordinates alongside  $R_o$  and  $r_o$ .

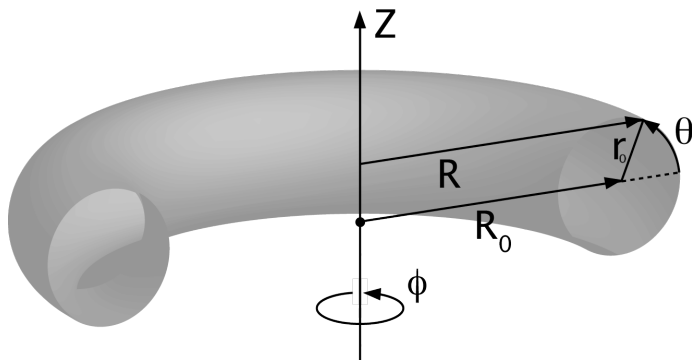


Figure 5: Geometry quantities  
(figure taken from [12])

### 2.2 Magnetic Fields

In order to sustain the burning plasma, energy generated by the fusion reactions must be greater than the lost energy. This relation is described by the **Lawson criterion**

$$n_i \cdot T_i \cdot \tau_E \geq \frac{12}{E_{ch}} \frac{k_B T_i^2}{\langle \sigma v \rangle} \quad (1)$$

where  $n_i$  is the ion density,  $T_i$  the ion temperature,  $\tau_E$  the energy confinement time and  $k_B$  the Boltzmann constant

$$k_B = 1.380649 \cdot 10^{-23} \text{ J K}^{-1} \quad (2)$$

$\langle \sigma v \rangle$  is called Reaction rate and is the product of the velocity dependend cross section and the particle speed.  $E_{ch}$  defines the energy of charged fusion products and measures 3.5 MeV in the context of the Deuterium-Tritium reaction. The Lawson criterion basically means that enough particles with certain energy need to be trapped long enough to keep the plasma burning.[13]

Confinement can be achieved using the **Lorentz force**: Moving charges in a magnetic field will encounter a force in a direction that is perpendicular to both the particle's

velocity vector and the magnetic field vector. Since not only magnetic but also electric fields can interact with charges, the formal equation extends to

$$\vec{F}_L = q \cdot (\vec{E} + \vec{v} \times \vec{B}) \quad (3)$$

where  $q$  is the charge,  $\vec{E}$  the electric field vector,  $\vec{v}$  the vector of the particle's velocity and  $\vec{B}$  the magnetic field vector. This is also the reason why trajectories of particles that follow the magnetic field lines appear as a helix, known as **gyration**.

The **poloidal magnetic field** is produced by both inner and outer poloidal magnetic field coils. These coils play a crucial role in sculpting the plasma into the desired configuration and regulating its vertical position. As a result, at ASDEX Upgrade, for example, different electrical current can be applied, enabling the investigation of diverse magnetic configurations. Nevertheless, the primary source of the poloidal magnetic field stems from the electrical current circulating through the tokamak reactor. Clearly, the magnetic field lines are denser closer to the tokamak center, which results in stronger field strength and unbalanced confinement. To overcome this issue, we incorporate toroidal magnetic field coils that provide the tokamak with a **toroidal magnetic field**.

Due to superposition the combination of the toroidal and poloidal magnetic fields results in a strongly twisted magnetic field. Figure 6 displays how the poloidal magnetic field in blue color and the toroidal magnetic field in yellow color result in a twisted magnetic field in green color.

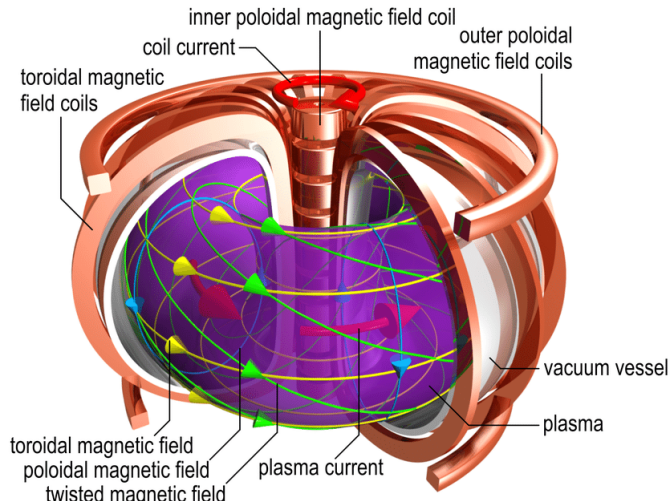


Figure 6: tokamak magnetic fields  
(figure taken from [14])

## 2.3 Heating and Fueling

### Heating

To regulate plasma temperature in tokamak reactors, a range of heating techniques are employed at the ASDEX Upgrade machine. One of these methods, neutral particle injection, involves the injection of inert, nonflammable gas into the plasma through two large ports. This increases the overall particle density, resulting in more particle

collisions and a rise in temperature. This technique is capable of delivering up to 20 MW of power.

In addition to neutral particle injection, high-frequency heating and microwave heating are also employed at ASDEX Upgrade. These methods can deliver up to 6 MW and 8 MW of power, respectively. [15][10]

## Fueling

Similar to a car, a fusion reactor continuously consumes fuel and needs a constant supply of new fuel. There are primarily two methods of refueling a fusion reactor impacting different regimes: **gas puffing** and **pellet injection**.

Gas puffing involves injecting gas into the plasma, which has an impact on the density at the edge of the plasma. On the other hand, pellet injection involves inserting frozen hydrogen pellets into the plasma, which can last longer and are more likely to reach the inner plasma. Therefore these processes are also interesting with respect to the bootstrap current. [15]

## 2.4 Diagnostics and IDA

Nowadays, fusion machines are equipped with a variety of diagnostics, each with its own function and unique advantages. By utilizing these different methods, complementary and redundant data can be gathered, resulting in increased spatial and temporal resolution of profiles and the ability to resolve data inconsistencies. To fully utilize the variety of heterogeneous diagnostics available, on ASDEX Upgrade a method called **Integrated Data Analysis (IDA)** that makes use of Bayesian probability theory, has been developed.

This approach utilizes a useful combination of data obtained from various measurement approaches, such as lithium beam emission spectroscopy (LIB), deuterium cyanide laser interferometry, electron cyclotron emission (ECE), and Thomson scattering spectroscopy, to effectively analyze and estimate the electron density and temperature profiles of a plasma. The application of these different measurement techniques allows for a simultaneous estimation of these plasma properties, even with high spatial and temporal resolution, thereby providing the basis for a comprehensive understanding of the plasma dynamics. [16]

## 2.5 Equilibrium

Having in mind the tokamak's axial symmetry, many investigations can be broken down from a three to a two dimensional problem by having a look at the tokamak's cross section. Some can even be broken further down to one dimension like the bootstrap current in this thesis.

### 2.5.1 Equations

In order to confine the plasma and keep it away from the walls, the magnetic fields need to meet the equilibrium conditions. These conditions result from coupling Navier-Stokes' and Maxwell's equations and lead to a formalism that describe the plasma

by magnetohydrodynamics. This formalism include macroscopic quantities such as density, velocity and temperature. Hence, it's possible to find a relation between the magnetic field and the pressure gradient. In the equilibrium state, forces of both plasma pressure and magnetic fields are in balance.

For an Equilibrium, the plasma must satisfy

$$\vec{\nabla}p = \vec{j} \times \vec{B} \quad (4)$$

where  $\vec{\nabla}p$  is the pressure gradient,  $\vec{j}$  the electric current density vector and  $\vec{B}$  the magnetic field vector and

$$\vec{\nabla} \times \vec{B} = \mu_0 \vec{j} \quad (5)$$

where  $\mu_0$  is the vacuum permeability. [7]

### 2.5.2 Magnetic Flux Surfaces

It can be seen that both the magnetic field lines ( $\vec{B} \times \vec{\nabla}p = 0$ ) and the direction of current flow ( $\vec{j} \times \vec{\nabla}p = 0$ ) lie on surfaces of constant pressure ( $\vec{\nabla}p = 0$ ). The magnetic flux through these surfaces is usually described with  $\Psi$  and will be constant on such a surface. It can be computed by using the *Grad-Shafranov* equation. [17][15]

As a result, a new coordinate  $\rho_{pol}$  is introduced that defines a new normalized plasma radius that is 0 in the plasma core and 1 at the last closed flux surface, the so-called **separatrix**. It is therefore defined as

$$\rho_{pol} = \sqrt{\frac{\Psi - \Psi_0}{\Psi_{sep} - \Psi_0}} \quad (6)$$

where  $\Psi_0$  is the value of the magnetic flux at the axis and  $\Psi_{sep}$  is the magnetic flux at the separatrix. The region even further out from the axis, behind the separatrix, is called SOL (Scrape-Off-Layer) where the magnetic flux surfaces are not closed, but end up on a target in the Divertor instead. Figure 7 displays a crosssection that shows the magnetic flux surfaces in blue and the target as a part of the divertor in red.

### 2.5.3 Density, Temperature and Pressure

As mentioned above, one of the main goals in fusion research is to achieve the Lawson criterion (1). The product  $n_i \cdot T_i$  can also be interpreted as the plasma pressure:

$$p = n_i \cdot 2k_B \cdot T \quad (7)$$

In equilibrium, due to constant pressure  $p$  on a certain flux surface the particles will distribute nearly instantaneously resulting on constant  $n_i$  and  $T_i$  on this flux surface. Note that the overall pressure is much higher in the center of the plasma which ultimately leads to a pressure gradient.

Additionally, a distinction can be made between **H-mode (high confinement mode)** and **L-mode (low confinement mode)**. **H-mode (L-mode)** is characterized by **high (low)** energy and particle confinement.

**H-mode** can be achieved if a certain heating threshold is exceeded. Hence, higher

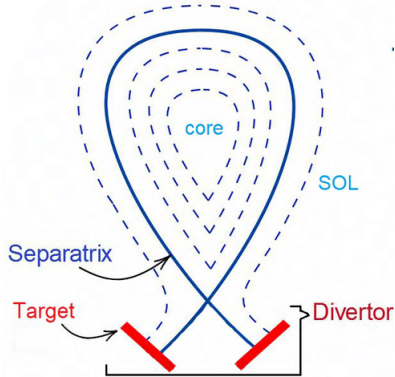


Figure 7: Tokamak cross section:  
The dashed lines represent the section of the magnetic surfaces.  
The last closed one is the Separatrix, the region behind the Scrape-Off-Layer (SOL).  
Magnetic surfaces in this region end up on a target in the Divertor.  
(figure taken from [18])

pressure gradients form and the whole plasma profile lifts on a so-called pedestal. Remarkably, the plasma's density and temperature does not decrease to almost zero at the edge. Instead, they cease declining at the pedestal (figure 8a). This behavior suggests the presence of a transport barrier (8b). This barrier is caused by a highly sheared azimuthal flow that prevents normal outward diffusion of plasma. [19][15]

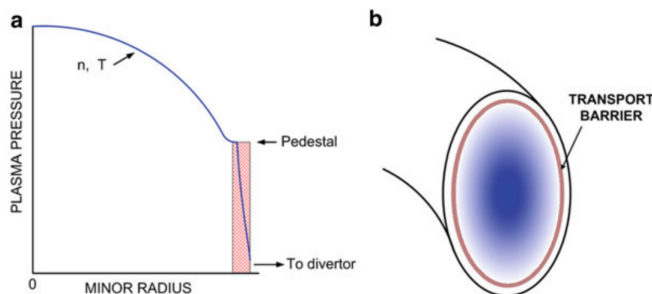


Figure 8: The H-mode barrier  
(figure taken from [7])

#### 2.5.4 Instabilities

In reality, plasma states are usually not in a perfect thermodynamic equilibrium, however, they can be considered to be in an equilibrium in a sense that all forces are in balance and a time-independent solution is possible. Thus, these systems contain free energy that causes the plasma waves to be self-excited and the equilibrium is unstable.<sup>1</sup> These instabilities will lower the amount of free energy in the system and at the same time help getting closer to a stable equilibrium back again. According to

<sup>1</sup>An illustrative analogy: Picture a pendulum composed of a rigid stick and a mass attached to it. This system exhibits two distinct equilibrium states:

(1) The stable equilibrium occurs when the pendulum hangs downward, aligned with the Earth's surface. If it experiences a slight external momentum, it will begin to swing but ultimately return to this position.

the type of free energy available to drive them there can be classified different types of instabilities.

Although **H-mode** provides better confinement for a fusion reactor, high pressure gradients at the pedestal will ultimately result in instabilities leading to quasi-periodic outbursts of energy from the plasma. These bursts are called edge localized mode (ELM). [7]

## 2.6 Collisionality

Collisionality is the measure of how frequent particle collisions occur. Given that the Bootstrap current is impacted by collisions occurring between trapped and passing particles (further elaboration will be provided in the following chapter), it's imperative to delve into the analysis of collisionality as well. The so-called plasma collisionality can be defined as

$$v_e^* = 6.921 \cdot 10^{-18} \frac{R_0 q_{95} n_e Z_{eff} \ln \Lambda_e}{\epsilon^{3/2} T_e^2} \quad (8)$$

where  $q_{95}$  is the safety factor at 95% flux,  $Z_{eff}$  the effective ionic charge and  $\ln \Lambda_e$  the Coulomb logarithm, a factor, by which small-angle collisions are more effective than large-angle collisions. The safety factor is a measure for the slope of a fieldline and is defined as

$$q = \frac{r_0 B_\phi}{R_0 B_\Theta} \quad (9)$$

where  $B_\phi$  ( $B_\Theta$ ) is the toroidal (poloidal) magnetic field. [15]

## 2.7 Transport

*Transport* in this context refers to the physical processes in which particles, momentum and energy are transported within the tokamak. A full understanding of transport enables us to understand the interaction between thermodynamic flows and forces. The dominant types of transport are turbulent transport and transport caused by collisions. For the latter one, there can be made a distinction between the **classical transport** (collective plasma movements) and the **neoclassical transport** (movement of single particles). The neoclassical transport typically much higher than the classical one and also crucial for the emergence of the Bootstrap current. Hence, it will be the focus in this thesis.

### 2.7.1 Trapped free Particles

Due to the inhomogeneity of the magnetic field ( $B \propto \frac{1}{R}$ ) and conservation of both energy and magnetic moment, particles will be trapped in a magnetic mirror on the outboard side if

$$\left( \frac{v_{||0}}{v_{\perp 0}} \right)^2 < \frac{B_{max} - B_{min}}{B_{min}} \approx 2\epsilon \quad (10)$$

---

(2) The unstable equilibrium arises when the pendulum points upward, opposite to the Earth's surface. This is an extremely delicate position, as the pendulum can only rest there momentarily before any perturbation causes it to deviate.

where  $v_{\parallel 0}$  ( $v_{\perp 0}$ ) is the particle's velocity vector components parallel (perpendicular) to the magnetic field  $B$  and  $\epsilon$  the inverse aspect ratio (see 2.1). Moreover,  $B_{\min}$  ( $B_{\max}$ ) is the minimum (maximum) magnetic field strength on the magnetic surface. Projecting these trajectories to the poloidal plane one can see the shape looks like a banana why it's called **banana orbits**. Figure 9 displays such banana trajectories alongside the separatrix. The trapped particles, however, don't follow straight lines but have a

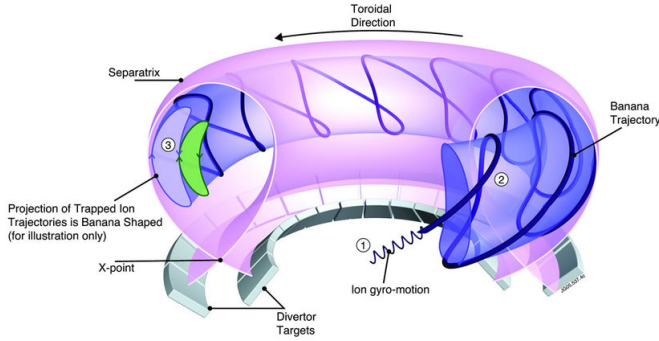


Figure 9: Trajectory of a trapped particles  
(figure taken from [20])

drift in vertical direction caused by the inhomogeneity of the magnetic field. Using the approximation  $B_t \approx B$  this results in a radial width

$$\omega \approx \frac{mcv_{\parallel}}{eB_p} \quad (11)$$

where  $m$  is the mass and  $v_{\parallel}$  the parallel velocity component of the particle,  $c$  speed of light in vacuum,  $e$  electronvolt and  $B_p$  ( $B_t$ ) the poloidal (toroidal) magnetic field.

## 2.7.2 Banana Currents

For a moment, we consider two trapped ions with the same energy and magnetic moment that start from the same point on the magnetic surface with a different sign of the parallel velocity. The ion with negative (positive) parallel velocity drifts inwards (outwards) resulting in a smaller (larger) radius of this orbit compared to the one of the considered flux surface. Thus, if a radial density gradient exists (true in most cases), this orbit will be populated more (less) compared to the one of the flux surface where the particle started. Ultimately, this results in an asymmetry in the velocity distribution, which means, however, that trapped particles will rather have negative than positive parallel velocity. Due to the charge dependency of the Lorentz force (see equation 3) this behavior is contrary if one considers electrons instead of ions. In other words, the drifts of the electrons is in the opposite direction plus, the asymmetry in the velocity distribution has the opposite sign. Figure 10 displays the asymmetric distribution of trapped particles.

Finally, the magnitude of the **banana current**  $J_B$  can be estimated resulting from the surplus of particles going in the direction of the current

$$\delta n_t = \omega \frac{dn_t}{dr}$$

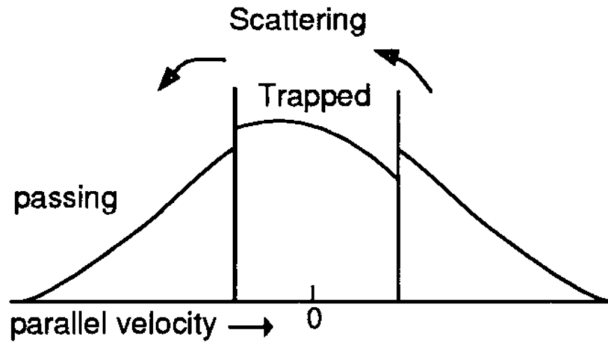


Figure 10: Asymmetric distribution of trapped particles  
(figure taken from [21])

where  $n_t \approx \sqrt{\epsilon}n$  is the trapped particle density times their average parallel velocity

$$v_{\parallel} \approx \sqrt{\epsilon}v_{\text{th}}$$

with  $v_{\text{th}} = 2T/m$  being the thermal velocity and  $\epsilon$  the inverse aspect ratio. The formulas above lead to

$$n_i u_{\parallel i, \text{trapped}} = \epsilon^{3/2} \frac{cT}{eB_p} \frac{dn}{dr} \quad \rightarrow \quad j_B = \frac{ce^{3/2}T}{B_p} \frac{dn}{dr} \quad (12)$$

including  $u_{\parallel i, \text{trapped}}$ ,  $c$ ,  $T$  and  $B_p$  and the direction of the current  $dn/dr$ . [21][17]

### 3 Bootstrap Current

From what has been explained so far it's clear that one wants to have high currents in the tokamak reactor to ensure strong confinement and therefore have higher chance of meeting the Lawson criterion that essentially requires the machine to maintain itself. Supplying the tokamak with more external energy would have counter productive effects because of the definition of the Lawson criterion (equation 1). Thus, we need to maximise the currents that occurs in the plasma naturally. One of them is the bootstrap current that will be explained in the following.

#### 3.1 Computational Methods

There are different approaches on how to calculate the bootstrap current. By the reason of the complexity of fusion machines and their occurring effects, one can consider to make approximations, as they will be sufficient and lead to an overall clearer understanding in certain cases despite possible loss of in-depth details. However, know-how of physics in tokamak reactors has improved a lot over the last decades, why results from modern approaches are more accurate than the ones resulting from prior ones. In this paper, the computation of the bootstrap profiles were done with an approximate bootstrap calculation formula introduced by Arthur Peeters. [21] Later on the validity of this formula will be discussed in comparison with other versions.

#### 3.2 Collisions between Trapped and Passing Particles

The part that contributes most to the **bootstrap** current are mainly collisions between trapped and passing particles. As shown in section 2.7.2 the asymmetry in the velocity distribution leads to the fact, that more trapped ions move in negative than positive toroidal direction resulting in an asymmetry in the passing domains as well. By having a look at the relations

$$\tau_{ii} \ll \tau_{ie} \quad \tau_{ei} \ll \tau_{ee}$$

where  $\tau_{ii}/\tau_{ie}/\tau_{ee}/\tau_{ei}$  is the average time passing by between an ion-ion / ion-electron / electron-electron / electron-ion collision, one can see, both ions and electrons most likely collide among ions. Due to the fact, that an electron will lose most of its momentum when colliding with an ion while ions colliding with ions keep their momentum on average, the velocity distribution is shifted from both ions and electrons but more likely the electrons, leading to the distribution function shown in figure 11. For this reason it's clear that the passing particles also contribute to the bootstrap current due to collisions with trapped ones. [21]

#### Changing Perspective to a Fluid Picture

A passing particle must be scattered at an angle of around 90 degrees to enter the trapped particle regime, but only  $\sqrt{\epsilon}$  of its original momentum will be transferred due to  $v_{||} \approx \sqrt{\epsilon} v_{th}$  (section 2.7.2) on the one hand and the reduction of momentum during

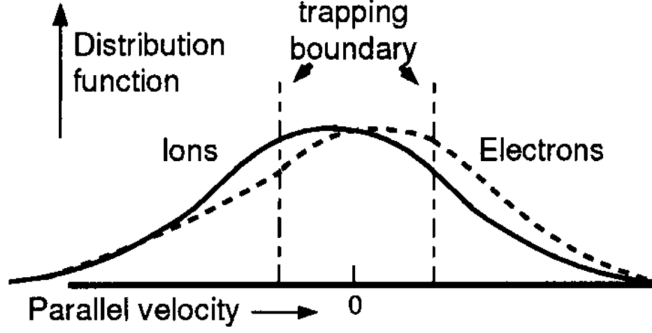


Figure 11: Diagram of the distribution function of ions and electrons  
(figure taken from [21])

the scattering process on the other one. As a consequence, the parallel velocity for particles in the passing domain will change from equation 12 to

$$n_i \frac{\partial u_{\parallel i,p}}{\partial t} = \frac{v_{ii}}{\epsilon} \frac{e^{3/2} c T}{e B_p} \frac{dn}{dr} \quad (13)$$

where  $\epsilon/v_{ii}$  is the typical timescale for trapped ions giving their momentum to the passing ions.  $v$  is the frequency for a 90 degree angle scattering.

At this point it can help to switch the perspective to the plasma from particles picture to a fluid one. Hence, we can compare equation 13 with the momentum balance in its most general form:

$$mn\vec{B} \cdot \frac{du}{dt} = -\vec{B} \cdot \nabla p + en\vec{B} \cdot \vec{E} - \vec{B} \cdot \nabla \cdot \bar{\pi} + \vec{B} \cdot \vec{F}$$

Since in the derivation above we did not consider the parallel pressure ( $\vec{B} \cdot \nabla p$ ), the parallel electric field ( $\vec{B} \cdot \vec{E}$ ) or friction ( $\vec{B} \cdot \vec{F}$ ), by using equation 13 one is getting an equation for the viscous force

$$-\vec{B} \cdot \nabla \cdot \bar{\pi} = mn\sqrt{\epsilon} v_{ii} \vec{B} \left[ \frac{cT}{enB_p} \frac{dn}{dr} - u_{\parallel} \right] \quad (14)$$

The last term in the brackets is proportional to the poloidal fluid velocity  $V_p$ , which is the sum of: (1) poloidal components of parallel velocity and (2) diamagnetic velocity ( $v_{dia}$ ), which lies inside the flux surface and is perpendicular to the magnetic field:

$$v_{dia} = -\frac{cT}{enB} \frac{dn}{dr} \quad \rightarrow \quad V_p = \frac{B_t}{B} v_{dia} + \frac{B_p}{B} u_{\parallel} \approx -\frac{B_p}{B} \left[ \frac{cT}{enB_p} \frac{dn}{dr} - u_{\parallel} \right]$$

By using this relation in equation 14 one will see

$$mn\vec{B} \cdot \frac{du_{\parallel}}{dt} = -\vec{B} \cdot \nabla \cdot \bar{\pi} = -mn\sqrt{\epsilon} v_{ii} B^2 \frac{V_p}{B_p} = -\mu_i B^2 \frac{V_p}{B_p}$$

where  $\mu_i = mn\sqrt{\epsilon}v_{ii}$  is the viscosity coefficient for ions.

Thus, it can be seen that the density gradient leads to a diamagnetic velocity in the flux surface which has a poloidal component. However, the magnetic field strength changes in this direction resulting in a viscous force. This force damps the poloidal movement by building up a parallel velocity until the poloidal component of the velocity cancels the poloidal component of the diamagnetic velocity.

Hence, the resulting total velocity is in the direction of the symmetry of the system (toroidal) and independent of the field strength. The viscous force we found in the fluid picture can be interpreted as a result from the friction between trapped and passing particles. As seen in section 2.7.1, trapped particles don't rotate in poloidal direction, which is the same result that is obtained from the fluid picture which shows its equivalence. [21]

## Using Steady-state Equations

The steady-state equations for parallel velocity of the ions and electrons can be written as

$$u_i \left[ \frac{cT}{en_i B_p} \frac{dn_i}{dr} - u_{\parallel i} \right] = 0 \quad u_e \left[ \frac{cT}{en_e B_p} \frac{dn_e}{dr} - u_{\parallel e} \right] = l_{ei}(u_{\parallel e} - u_{\parallel i}) \quad (15)$$

where - as mentioned above - the inhomogeneous term in the electrons equation comes from friction with ions. Thus, the viscosity coefficient for electron  $\mu_e$  reads as

$$\mu_e = m_e n_e \sqrt{\epsilon} v_{ei}$$

where apparently we ignore electron-electron collision for simplicity. Moreover, we the electron ion friction coefficient as

$$l_{ei} = m_e n_e v_{ei}$$

By directly solving the equations 15 one gets

$$u_{\parallel i} = \frac{cT}{en_i B_p} \frac{dn_i}{dr} \quad u_{\parallel e} = \frac{l_{ei}}{\mu_e + l_{ei}} \frac{cT}{en_i B_p} \frac{dn_i}{dr} - \frac{\mu_e}{\mu_e + l_{ei}} \frac{cT}{en_e B_p} \frac{dn_e}{dr}$$

If the inverse aspect ratio  $\epsilon$  is small, then  $\mu_e \ll l_{ei}$  meaning that electrons move mostly with the ions.

The difference in velocity yields the **bootstrap current**  $J_{BS}$ :

$$J_{BS} = \frac{cT}{B_p} \frac{\mu_e}{\mu_e + m_e n_e v_{ei}} \left[ \frac{dn_i}{dr} + \frac{dn_e}{dr} \right] \approx \sqrt{\epsilon} \frac{cT}{B_p} \left[ \frac{dn_i}{dr} + \frac{dn_e}{dr} \right] \quad (16)$$

Comparing 16 with 12 makes clear that the Bootstrap current is  $1/\epsilon$  larger than the Banana current  $J_B$  (equation 12). [21]

### 3.3 Accuracy Evaluation and Further Improvement

As a matter of fact, the complete Bootstrap Current theory is much more complicated. However, as mentioned in the introduction of this section there are several approximations one can utilize to obtain a simple but at the same time sufficient formula for specific use cases. In the following there will be listed a few points that are not considered in this simplified analysis:

- The *diamagnetic velocity* is also proportional to the pressure gradient and not just the density gradient
- Beside the diamagnetic velocity there is also a *diamagnetic heat flux* and a *heat viscous force* driving parallel heat fluxes similarly like the viscosity does for the parallel velocity. Diamagnetic heat flux can also affect the particle momentum.
- A similar coupling can be found for the viscous force which cannot be expressed entirely in the poloidal velocity but to which the poloidal heat flux also contributes.

Considering all these additional circumstances, one would get a set of linear equations. The most general form of the theory is formulated for arbitrary toroidally symmetric geometry. Consequently, the label of the flux surface can be given by the poloidal flux  $\Psi_p$ . To lowest order in  $\epsilon$  this yields

$$J_{BS} = -\sqrt{b} \frac{RB_t}{B_0} \left[ 2.44(T_e + T_i) \frac{dn}{d\Psi_p} + 0.69n \frac{dT_e}{d\Psi_p} - 0.42n \frac{dT_i}{d\Psi_p} \right] \quad (17)$$

with  $b = (B_{\max} - B_{\min})/(B_{\max} + B_{\min})$ . [21] It can be seen that the density gradient plays a more significant role than the temperature gradients, because of the prefactor. Also the ion temperature drives a current in the opposite direction. However, this is only true close to the axis, because finite  $\epsilon$  effects cause the term to change sign in regimes further away from the axis. General equations that include finite  $\epsilon$  effects and arbitrary ion charge can be found in [22]. [21]

### 3.4 Comparison with other Models

As mentioned above several approximations have been made to get to get an easier to understand picture of the Bootstrap current. However, for a precise computation the drift-kinetic-Poisson equations has to be solved completely, which is not an easy task. In the following, other approaches will be discussed that provide exact results.

#### 3.4.1 Sauter Model

The **Sauter Model** basically consists of a set of relatively simple analytic formulae that are obtained by fitting to the numerical results of two Fokker-Planck solvers <sup>2</sup> called *CQL3D* and *CQLP*. This model depends only on three parameters relevant in neoclassical transport:

---

<sup>2</sup>Fokker-Planck refers to the Fokker-Planck collision operator that can be seen as the sum of single collision possibilities of a incoming particle species  $\sigma$  hitting an environment built up of a particle species  $\gamma$ .

- $f_{\text{trap}}$  - fraction of trapped particles
- $v_{\sigma}^*$  - collisionality of the species  $\sigma$
- $Z_{\text{eff}}$  - effective charge number

By solving the Fokker-Planck equation with linearized collision operator<sup>3</sup> and considering the exact axisymmetric magnetic configurations of the flux surfaces it is possible to calculate the bootstrap current density. Due to the simplification of the collision operator in the CQLP code and the limited computational power available, inaccuracies in the results are inevitable. [23]

### 3.4.2 NEO

The recently developed Eulerian code **NEO** solves the first-order drift-kinetic equations. The drift-kinetic equation (DKE) follow from the kinetic equation that describe the plasma movement and introduces an ordering parameter  $\sigma$ . It plays a fundamental role in calculating the neoclassical transport, however, it is a challenging task to solve it. Beyond the drift-ordering, NEO does not use any further approximations, but the full linearized Fokker-Planck collision operator in order to describe collision dynamics. [24]

### 3.4.3 Integrating NEO with the Sauter Model

**Andreas Redl** used the numerical results from the NEO code in order to refine the analytical formulae for the bootstrap current. This more accurate revised set now agrees with the results from the NEO code within 5% and therefore represents a significant improvement over the original Sauter model.

Thus, the flux surface averaged parallel current is given by

$$\langle j_{\parallel B} \rangle = \sigma_{\text{neo}} \langle E_{\parallel} B \rangle - I(\Psi) \left( p \mathcal{L}_{31} \frac{\partial \ln n}{\partial \Psi} + p_e (\mathcal{L}_{31} + \mathcal{L}_{32}) \frac{\partial \ln T_e}{\partial \Psi} + p_i (\mathcal{L}_{31} + \mathcal{L}_{34}\alpha) \frac{\partial \ln T_i}{\partial \Psi} \right) \quad (18)$$

where  $\mathcal{L}_{31}$ ,  $\mathcal{L}_{32}$ ,  $\mathcal{L}_{34}$ ,  $\alpha$  are the bootstrap current coefficients relative to the density-, the electron-, and the ion temperature gradients that ultimately impact the pressure and  $\sigma_{\text{neo}}$  the neoclassical resistivity. Note, that the dependencies of these coefficients are still the same as in the Sauter Model (see section 3.4.1). [25]

---

<sup>3</sup>A collision opearator represents the rate of change of the particle distribution due to collisions

## 4 Manipulation of Density Profiles

In equation 17, the Bootstrap current relies on multiple factors, including density, temperature and their corresponding gradients. By exclusively altering the density profile while keeping all other factors constant, a thorough comprehension of its sole influence on the Bootstrap current can be analyzed. As this approach is purely theoretical, these alterations are herein referred to as *manipulations*.

### 4.1 Original Density Profile

The original data recorded by the ASDEX Upgrade system is loaded and the density values are saved in a Python list. The list contains 200 interpolation points of the density, starting from the plasma center and extending to approximately  $\rho_{pol} = 1.25$ . Each of these 200 points holds 6999 values to show the temporal progression. A typical Density profile, along with the gradient, is plotted and shown in figure 12.

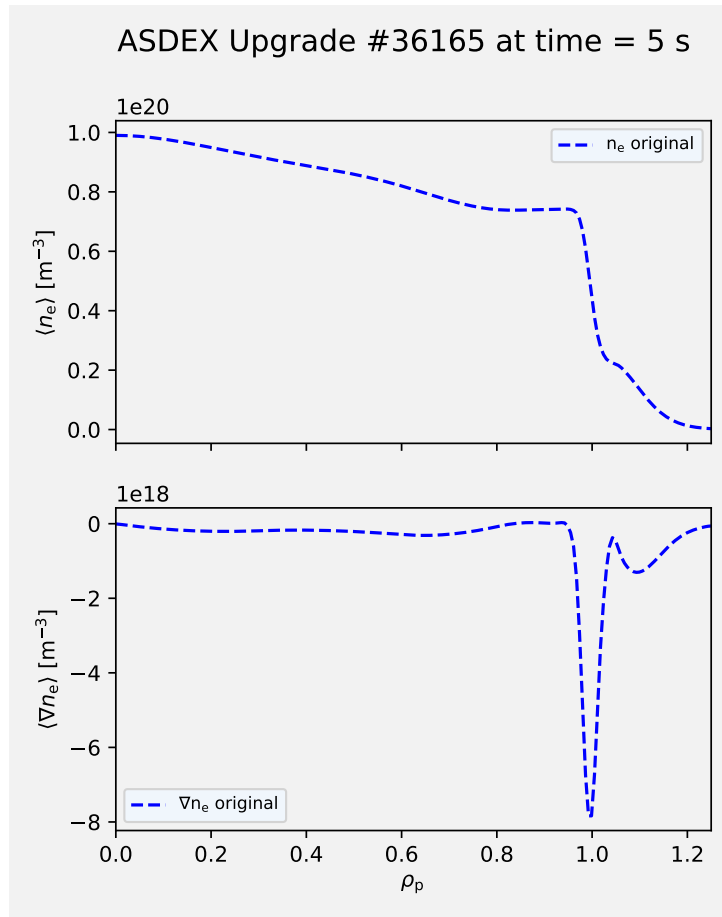


Figure 12: Radial density profile plotted along with the gradient

### 4.2 Manipulation methods

I developed a density manipulator feature that enables us to adjust both the position and steepness of the density profile by using manipulation functions described

below.<sup>4</sup> Although it is generally possible to combine these functions - i.e. execute multiple manipulations on the same density profile, for simplicity, we treat their impacts separately.

Additionally, since the bootstrap equation 17 emphasizes the significance of density gradients, we also display them correspondingly. In the following, four implemented methods are introduced.

---

<sup>4</sup>These manipulation functions only take a scaling parameter as an input. Further insight can be gained from the source code which is provided in the appendix A.1

#### 4.2.1 Constant Horizontal Shift

This method shifts the entire density profile by a constant value in the horizontal direction. Consequently, the gradient will also shift by the same amount, which is displayed in figure 13.

This transformation can be described with

$$n_{man}(\rho) = n_{orig}(\rho - d)$$

where  $n_{man}$  stands for the manipulated and  $n_{orig}$  for the original density profile.  $d$  is the constant horizontal offset and can be set by the scaling parameter.

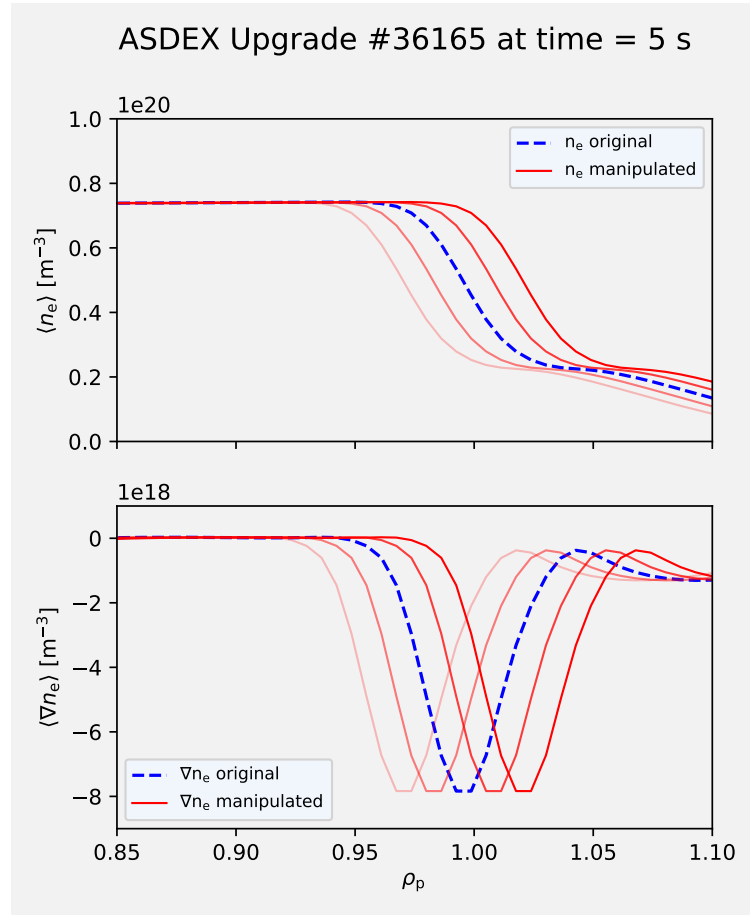


Figure 13: Radial density profile and corresponding gradient where *Constant Horizontal Shift* manipulation is applied

#### 4.2.2 Constant Vertical Shift

This method is quite similar to 4.2.1 but it shifts the profile in the vertical direction instead of the horizontal one. Therefore, the gradient remains completely unchanged, as the derivative of a function ignores constant offset values as shown in figure 14. The manipulated density function can be defined as

$$n_{man}(\rho) = n_{orig}(\rho) + t$$

where  $t$  is the constant vertical offset and can be set by the scaling parameter.

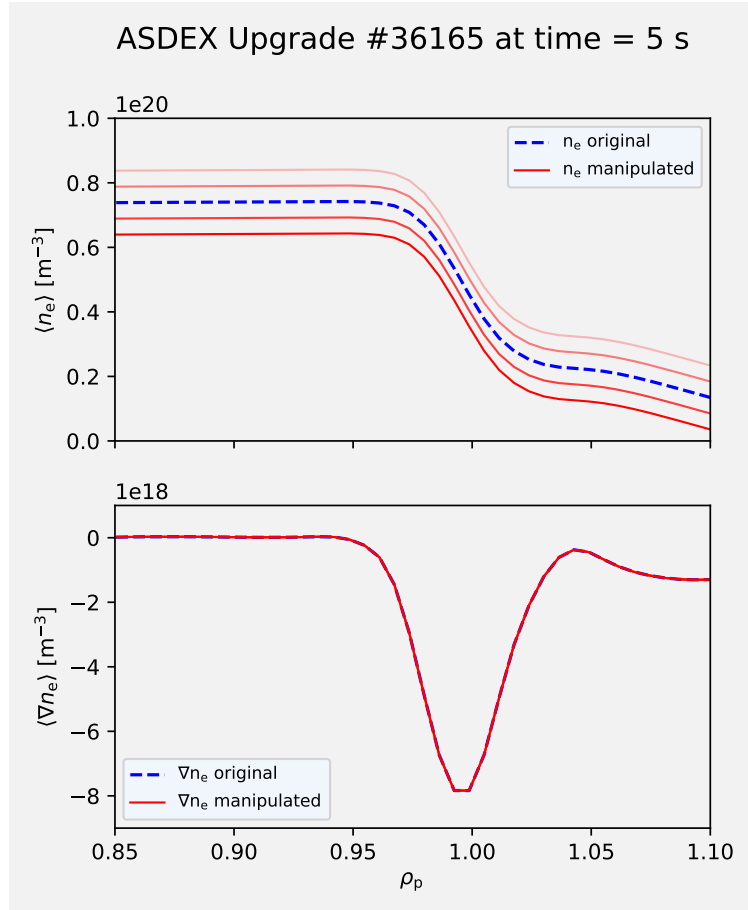


Figure 14: Radial density profile and corresponding gradient where *Constant Vertical Shift* manipulation is applied

### 4.2.3 Pedestal's Height Shift

This method modifies the Pedestal's height by shifting the graph along a linear trajectory, either upwards or downwards from the Inflection Point (*Wendepunkt*). As the Pedestal's level increases, the gradient widens, and conversely, it narrows as the pedestal's height decreases, which is shown in figure 15.

This transformation can be described as

$$n_{man}(\rho) = \begin{cases} n_{orig}(\rho - a) + b, & \text{if } \rho \leq \rho_0 \\ n_{orig}(\rho), & \text{if } \rho > \rho_0 \end{cases}$$

with  $a, b \in \mathbb{R}$  and  $\rho_0$  being the Inflection Point.  $\rho_0$  is determined through the following relation:

$$\frac{d^2 n}{d\rho^2}(\rho_0) = 0.$$

Additionally, the value of both  $a$  and  $b$  is influenced by the choice of the scaling parameter.

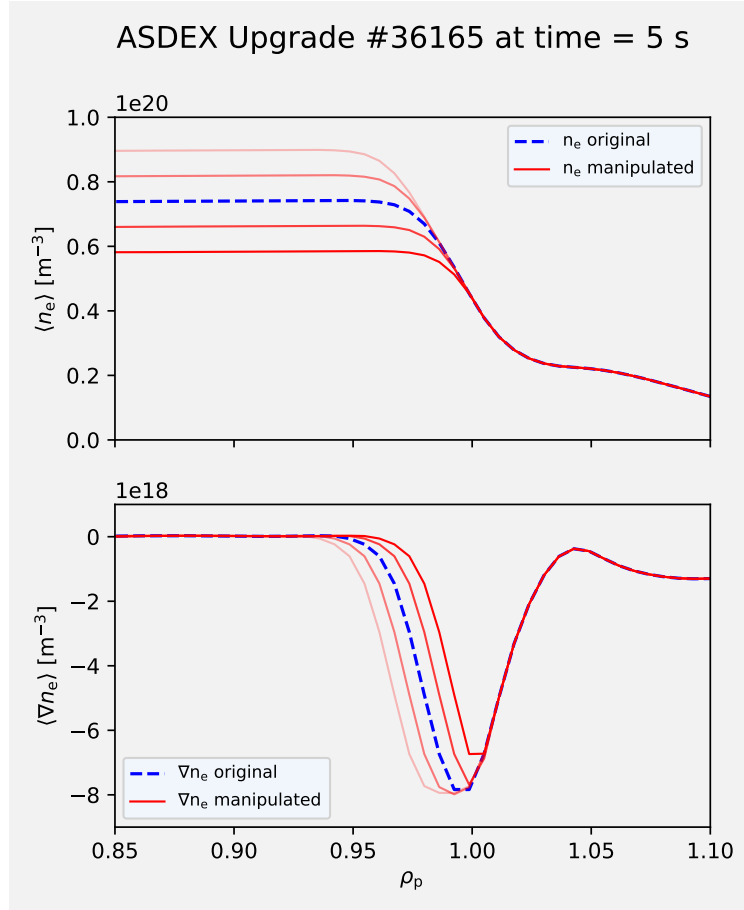


Figure 15: Radial density profile and corresponding gradient where *Pedestal's Height Shift* manipulation is applied

#### 4.2.4 Pedestal Steepness Shift

This method effectively modifies the steepness of the Pedestal by progressively increasing its size from an initial point  $\rho_0 > 0$  to  $\rho = 0$ . Consequently, the density gradient undergoes significant enlargement in both its overall magnitude and, to a lesser extent, its width as one can see in figure 16.

To attain this gradual progression, a function is essential, one that yields exceedingly small values at the outset ( $0 << \rho < \rho_0$ ) and steadily rises for decreasing values ( $0 < \rho < \rho_0$ ). An ideal choice for this situation is the  $\arctan(x)$  function, which aligns seamlessly with the desired behavior due to its asymptotic approach toward  $\pi/2$ . However, some adjustments are needed to tailor it to the specific density profile cutoff.<sup>5</sup>

$$n_{man}(\rho) = \begin{cases} n_{orig}(\rho) + \arctan_{modified}(\rho), & \text{if } \rho \leq \rho_0 \\ n_{orig}(\rho), & \text{if } \rho > \rho_0 \end{cases}$$

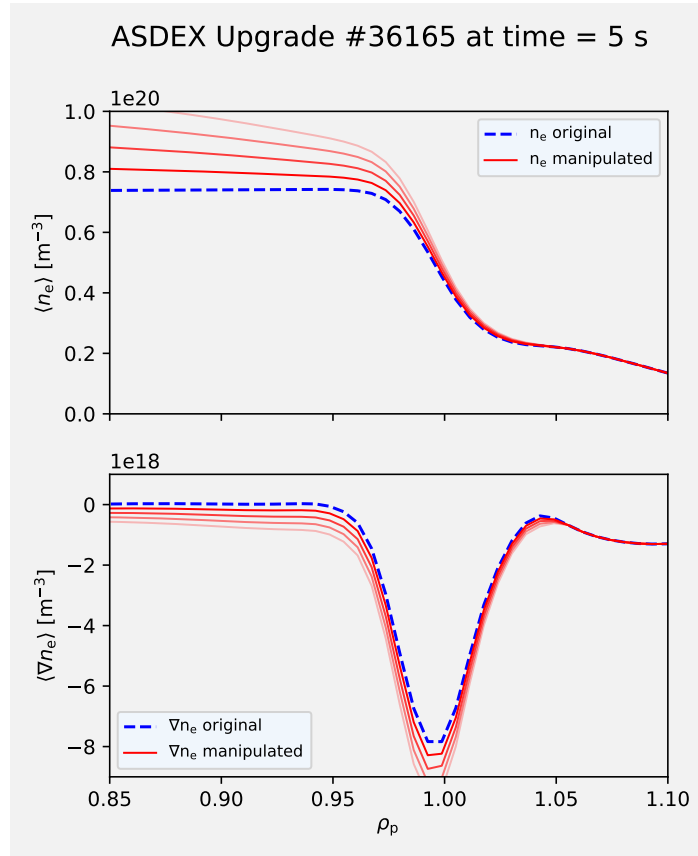


Figure 16: Radial density profile and corresponding gradient where *Pedestal Steepness Shift* manipulation is applied

<sup>5</sup>see A.1 for implementation details

## 5 Impact on the Bootstrap Current

In this chapter, manipulated density profile from the previous section will be used to analyze their impact on the Bootstrap current.

### 5.1 Original Bootstrap Current Profile

First, using the original density data from IDA that has been shown in figure 12, the original Bootstrap Current is computed with Peeters' formula (see equation 17) and visualized in figure 17.

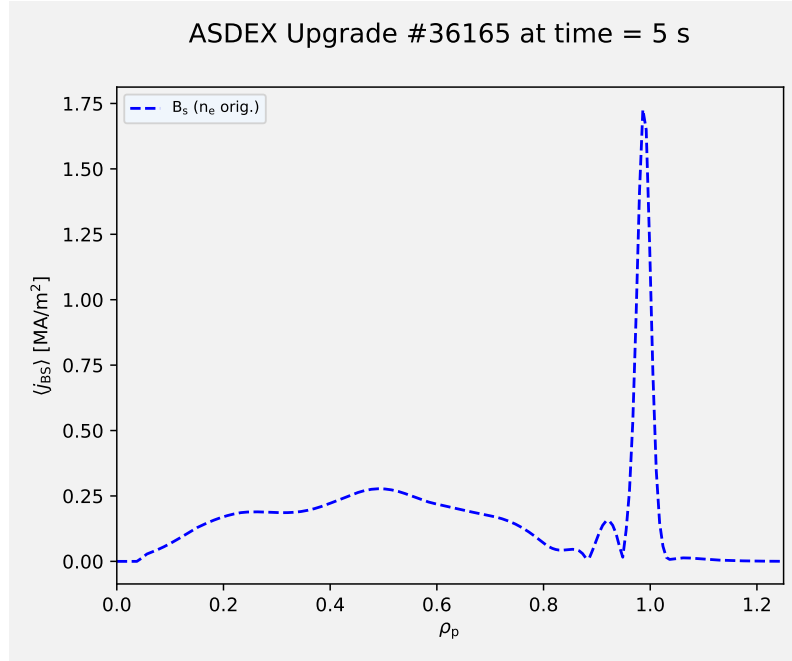


Figure 17: Radial Bootstrap current profile

### 5.2 Determination of the Bootstrap Current using manipulated Density Profiles

Secondly, we recalculate the Bootstrap Current using each modified density profile (refer to section 4.2) and present it alongside collisionality  $\nu_*$ , a critical factor influencing the Bootstrap Current. Additionally, we provide the Electron Temperature  $T_e$  and Ion Temperature  $T_i$  along with their respective gradients for reference.

### 5.2.1 Using Constant Horizontal Shift Manipulation

As shown in Figure 18, shifting a density profile to the right moves the bootstrap current peak to the right with a reduced amplitude, while a leftward shift raises the peak to the left. This asymmetric behavior can be attributed to the interplay between the density profile and the temperature gradient, as per Equation 17.

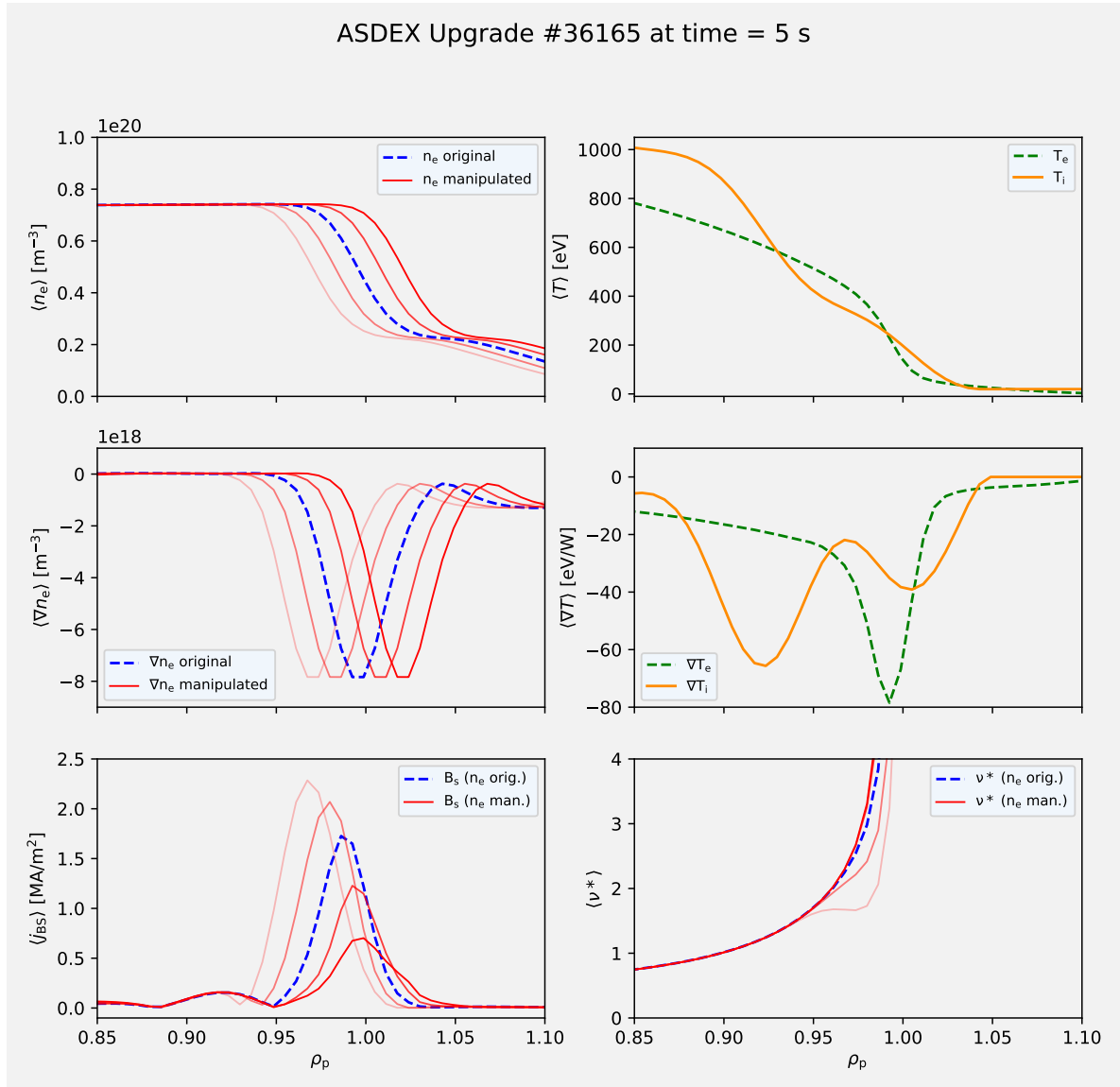


Figure 18: Radial density, density gradient, Bootstrap current and collisionality profile and radial ion/electron temperature profiles with their gradients under the impact of a *Constant Horizontal Shift* Manipulation described in section 4.2.1.

### 5.2.2 Using Constant Vertical Shift Manipulation

As illustrated in Figure 19, when the density profile undergoes vertical shifts, the bootstrap current exhibits relatively minor fluctuations in magnitude. An upward shift results in a heightened peak, while a downward shift leads to a diminished peak. Nonetheless, it's important to note that these shifts also cause a slight modification in collisionality: An increased quantity of electrons raises the likelihood of collisions between them, and conversely.

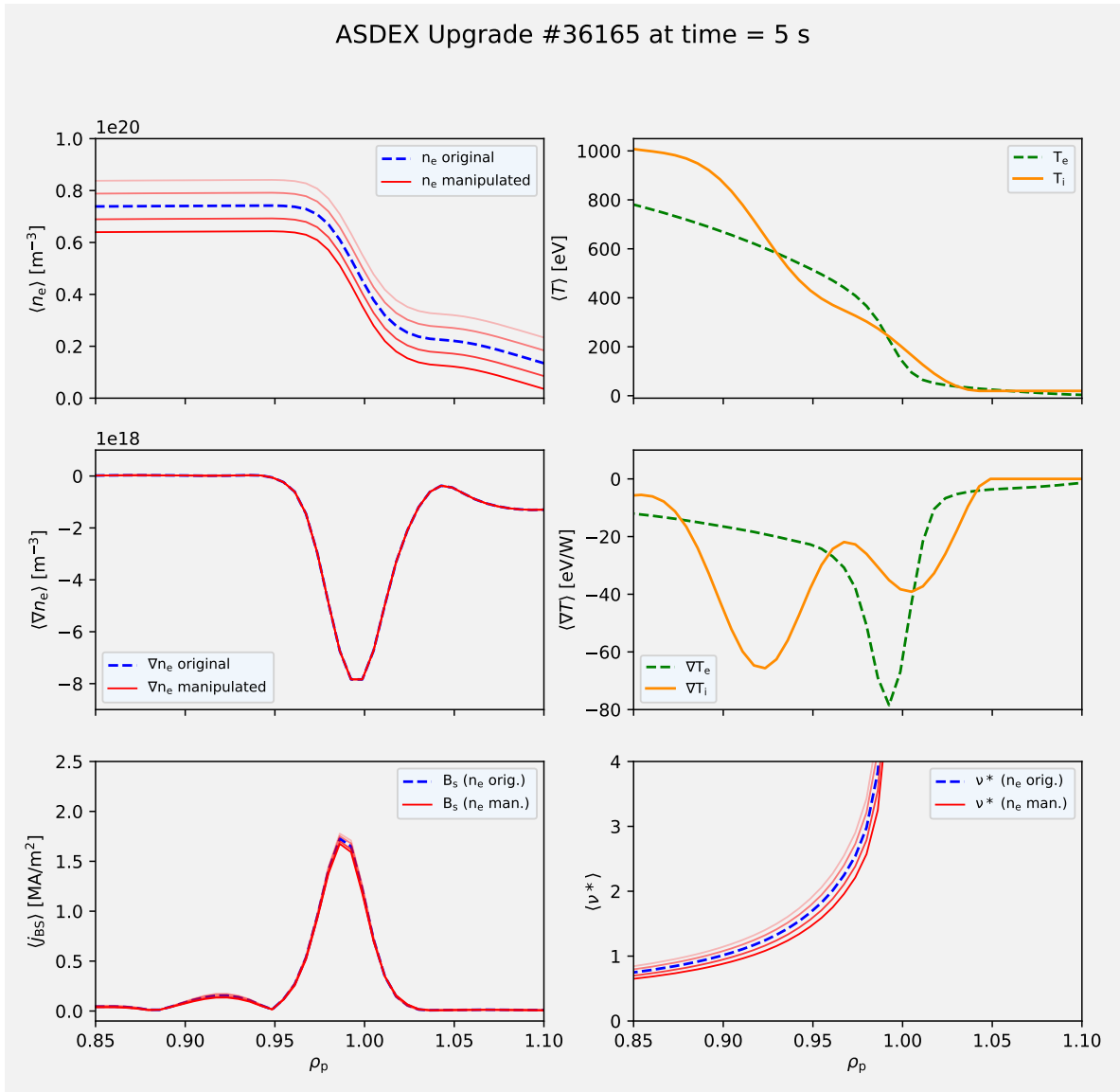


Figure 19: Radial density, density gradient, Bootstrap current and collisionality profile and radial ion/electron temperature profiles with their gradients under the impact of a *Constant Vertical Shift* Manipulation described in section 4.2.2.

### 5.2.3 Using Pedestal's Height Shift Manipulation

Figure 20 demonstrates that alterations in the Pedestal's Height result in variations in both the amplitude and width of the Bootstrap Current, accompanied by corresponding changes in collisionality within the Pedestal region.

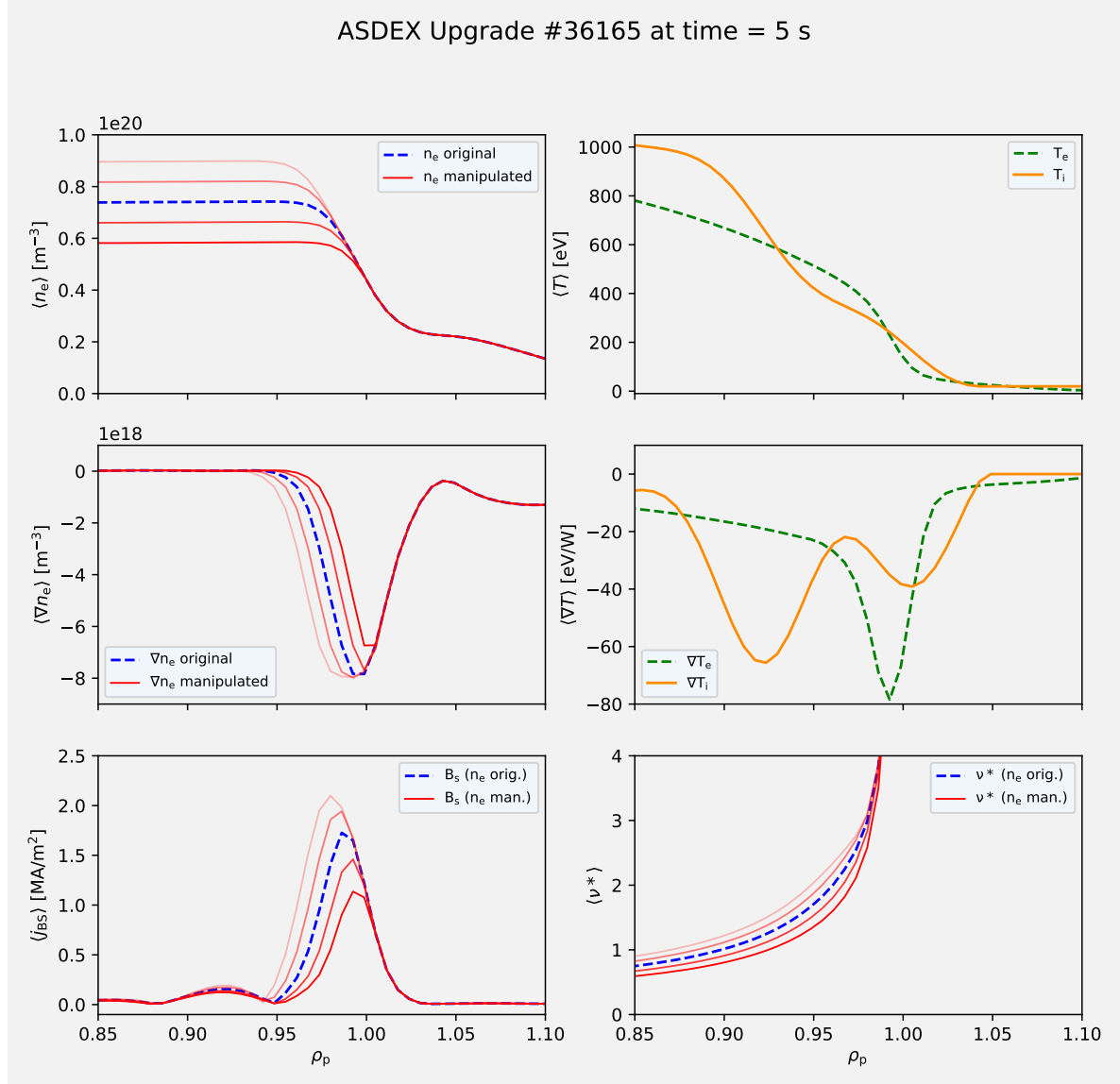


Figure 20: Radial density, density gradient, Bootstrap current and collisionality profile and radial ion/electron temperature profiles with their gradients under the impact of a *Pedestal's Height Shift* Manipulation described in section 4.2.3

### 5.2.4 Using Pedestal's Steepness Shift Manipulation

As depicted in Figure 21, the Bootstrap Current not only undergoes amplitude variations but also exhibits changes in its shape at lower rho values. This behavior can be attributed to the interplay between the density profile and the temperature gradient. Moreover, the collisionality increased as anticipated.

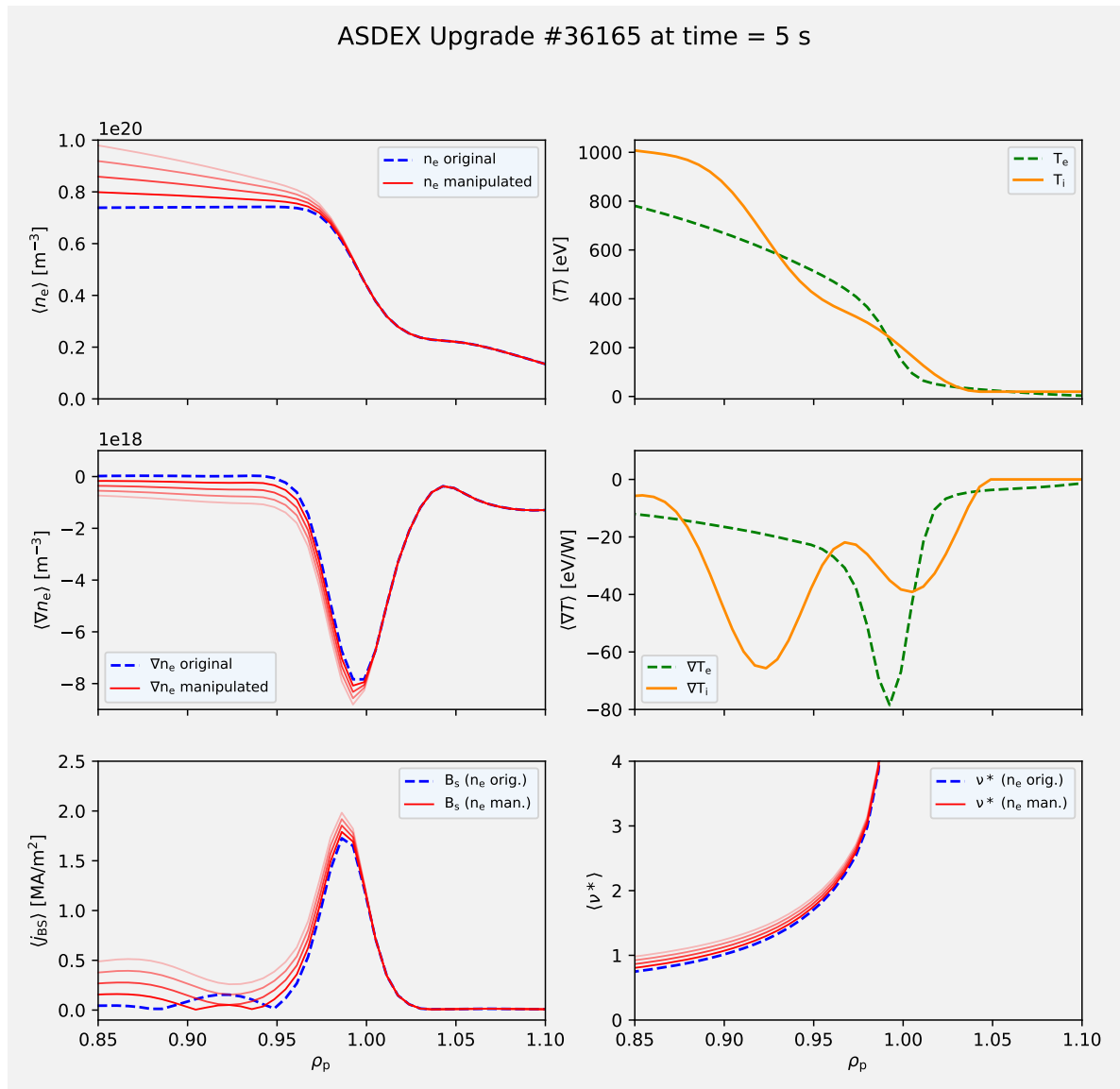


Figure 21: Radial density, density gradient, Bootstrap current and collisionality profile and radial ion/electron temperature profiles with their gradients under the impact of a *Pedestal's Steepness Shift* Manipulation described in section 4.2.4

## 6 Summary and Results

### Workflow summary

In this thesis, density profiles from ASDEX Upgrade experiments have been manipulated to investigate their impact on the Bootstrap current and the collisionality.

The Bootstrap current, as seen in section 3, is a self-generated current in tokamak reactors and of paramount importance and depends mainly on these factors:

- Density and corresponding gradient
- Temperature and corresponding gradient
- Collisionality of the particles
- Fraction of trapped particles

To tackle the intricate nature of the precise Bootstrap current calculation, an approximation formula devised by A.G. Peeters was employed in this thesis. This simplification allows for a concentrated analysis of how the density profile and its gradient directly impact the Bootstrap current, while maintaining the other listed parameters as constant.

The profile manipulation was achieved through a Python program (see appendix A.1) and encompasses four distinct methods (described in section 4.2):

- Constant Horizontal Shift
- Constant Vertical Shift
- Pedestal's Height Shift
- Pedestal Steepness Shift

Finally, the Bootstrap current has been recalculated for each of these methods, accompanied by temperature and collisionality profiles.

### Results

As anticipated, the *Constant Vertical Shift* manipulation of the density profile solely alters the peak size of the Bootstrap current (refer to section 5.2.2), leaving its horizontal position unchanged. Conversely, collisionality increases (decreases) for upward (downward) shifted density profiles. This shift impacts the particle count, affecting the average travel distance required for collisions to occur.

A more pronounced effect becomes evident when shifting the density gradient peak toward regions of higher temperature. The Bootstrap formula (equation 17) explains this: the density gradient, multiplied by the sum of ion and electron temperatures, significantly enhances the Bootstrap current when shifted toward the plasma core, where temperatures rise.

However, the most intriguing observation concerns collisionality: a leftward shift of

the density gradient, whether through *Constant Horizontal Shift* or *Pedestal's Height Shift* (refer to sections 5.2.1 and 5.2.3), leads to a corresponding shift in the Bootstrap current. Yet, collisionality decreases in the former and increases in the latter.

Hence, this implies that collisionality isn't the primary determinant of the Bootstrap current; instead, it's the density gradient in conjunction with the temperature profile.

In conclusion, enhancing simulation accuracy involves incorporating the precise Bootstrap computation formula in future research. Furthermore, these manipulation techniques exhibit potential for application in various scenarios where the individual impacts of density profiles are under scrutiny.

# A Appendix

## A.1 Source Code

The complete Python code (including the given examples shown above) is available on GitHub. Further details can be found in the *readme.md* file.

[https://github.com/SamuelLechner/BSC\\_Calc\\_Lechner](https://github.com/SamuelLechner/BSC_Calc_Lechner)

## Acronyms glossary

**n<sub>i</sub>** Ion Density

**T<sub>i</sub>** Ion Temperature

**T** Temperature

**p** Plasma pressure

**R<sub>o</sub>** Major Plasma Radius

**r<sub>o</sub>** Minor Plasma Radius

$\rho_{pol}$  Normalized Plasma Radius

$\Psi$  Magnetic Flux

**B<sub>p</sub>** Poloidal Magnetic Field

**L-mode** Low Confinement Mode

**H-mode** High Confinement Mode

**ELM** Edge Localized Mode

**SOL** Scrape Off Layer

**c** Speed of Light in Vacuum:  $3 \cdot 10^8$  m/s

$\epsilon$  Inverse Aspect Ratio

**j<sub>B</sub>** Bananca current

**u<sub>||i, trapped</sub>** Average parallel velocity of trapped ions

**u<sub>||i, p</sub>** Average parallel velocity of passing ions

$v_{th}$  Thermal velocity

$\mu_i$  Viscosity Coefficient for Ions

$\mu_e$  Viscosity Coefficient for Electrons

**J<sub>B</sub>** Banana Current

**J<sub>BS</sub>** Bootstrap Current

# List of Figures

1	Global primary energy consumption by source (figure taken from [1]) . . . . .	5
2	Fusion process on earth: When deuterium (upper left) and tritium (upper right) undergo fusion, they produce an $\alpha$ -particle and a high-energy neutron. (figure taken from [6]) . . . . .	7
3	Two different types of fusion reactors both run by the <i>Max-Planck-Institut für Plasmaphysik</i> . . . . .	8
4	Plasma vessel of ASDEX Upgrade (figure taken from [11]) . . . . .	8
5	Geometry quantities (figure taken from [12]) . . . . .	10
6	tokamak magnetic fields (figure taken from [14]) . . . . .	11
7	Tokamak cross section: The dashed lines represent the section of the magnetic surfaces. The last closed one is the Separatrix, the region behind the Scrape-Off-Layer (SOL). Magnetic surfaces in this region end up on a target in the Divertor. (figure taken from [18]) . . . . .	14
8	The H-mode barrier (figure taken from [7]) . . . . .	14
9	Trajectory of a trapped particles (figure taken from [20]) . . . . .	16
10	Asymmetric distribution of trapped particles (figure taken from [21]) . . . . .	17
11	Diagram of the distribution function of ions and electrons (figure taken from [21]) . . . . .	19
12	Radial density profile plotted along with the gradient . . . . .	23
13	Radial density profile and corresponding gradient where <i>Constant Horizontal Shift</i> manipulation is applied . . . . .	25
14	Radial density profile and corresponding gradient where <i>Constant Vertical Shift</i> manipulation is applied . . . . .	26
15	Radial density profile and corresponding gradient where <i>Pedestal's Height Shift</i> manipulation is applied . . . . .	27
16	Radial density profile and corresponding gradient where <i>Pedestal Steepness Shift</i> manipulation is applied . . . . .	28
17	Radial Bootstrap current profile . . . . .	29
18	Radial density, density gradient, Bootstrap current and collisionality profile and radial ion/electron temperature profiles with their gradients under the impact of a <i>Constant Horizontal Shift</i> Manipulation described in section 4.2.1. . . . .	30
19	Radial density, density gradient, Bootstrap current and collisionality profile and radial ion/electron temperature profiles with their gradients under the impact of a <i>Constant Vertical Shift</i> Manipulation described in section 4.2.2. . . . .	31
20	Radial density, density gradient, Bootstrap current and collisionality profile and radial ion/electron temperature profiles with their gradients under the impact of a <i>Pedestal's Height Shift</i> Manipulation described in section 4.2.3 . . . . .	32
21	Radial density, density gradient, Bootstrap current and collisionality profile and radial ion/electron temperature profiles with their gradients under the impact of a <i>Pedestal's Steepness Shift</i> Manipulation described in section 4.2.4 . . . . .	33

## References

- [1] Max Roser Hannah Ritchie. *Energy Production and Consumption*. 2022. URL: <https://ourworldindata.org/energy-production-consumption> (visited on 10/16/2022).
- [2] Myles R. Allen et al. "Warming caused by cumulative carbon emissions towards the trillionth tonne". In: *Nature* 458.7242 (Apr. 2009), pp. 1163–1166. DOI: 10.1038/nature08019. URL: <https://doi.org/10.1038/nature08019>.
- [3] Marilena Kampa and Elias Castanas. "Human health effects of air pollution". In: *Environmental Pollution* 151.2 (Jan. 2008), pp. 362–367. DOI: 10.1016/j.envpol.2007.06.012. URL: <https://doi.org/10.1016/j.envpol.2007.06.012>.
- [4] *When Fossil Fuels Run Out, What Then?* 2019. URL: <https://mahb.stanford.edu/library-item/fossil-fuels-run/> (visited on 04/12/2023).
- [5] *Climate change: EU moves to label nuclear and gas as sustainable despite internal row.* 2022. URL: <https://www.bbc.com/news/world-europe-60229199> (visited on 10/20/2022).
- [6] Wikimedia Commons. *D-t-fusion*. 2005. URL: <https://commons.wikimedia.org/wiki/File:D-t-fusion.png> (visited on 04/12/2023).
- [7] Francis F. Chen. *Introduction to Plasma Physics and Controlled Fusion (third edition)*. International series of monographs on physics. Springer International Publishing, 2016. ISBN: 978-3-319-22308-7.
- [8] *Sketch of the W7-X fusion device*. URL: [https://www.ipp.mpg.de/1456183/wendelstein\\_7\\_x](https://www.ipp.mpg.de/1456183/wendelstein_7_x) (visited on 04/12/2023).
- [9] *Sketch of the ASDEX Upgrade fusion device*. URL: [https://www.ipp.mpg.de/1471827/asdex\\_upgrade](https://www.ipp.mpg.de/1471827/asdex_upgrade) (visited on 04/12/2023).
- [10] *Introduction: The ASDEX Upgrade tokamak*. URL: <https://www.ipp.mpg.de/16208/einfuehrung> (visited on 11/24/2022).
- [11] Volker Rohde. *Plasma vessel of ASDEX Upgrade*. 2021. URL: [https://www.ipp.mpg.de/5035491/01\\_21](https://www.ipp.mpg.de/5035491/01_21) (visited on 11/25/2022).
- [12] FusionWiki. *Toroidal coordinates*. 2009. URL: [http://fusionwiki.ciemat.es/wiki/File:Toroidal\\_coordinates.png](http://fusionwiki.ciemat.es/wiki/File:Toroidal_coordinates.png) (visited on 10/20/2022).
- [13] J D Lawson. "Some Criteria for a Power Producing Thermonuclear Reactor". In: *Proceedings of the Physical Society. Section B* 70.1 (Jan. 1957), p. 6. DOI: 10.1088/0370-1301/70/1/303. URL: <https://dx.doi.org/10.1088/0370-1301/70/1/303>.
- [14] C. Brandt. *A schematic tokamak*. 2014. URL: [https://www.researchgate.net/figure/A-schematic-tokamak-figure-courtesy-of-C-Brandt\\_fig1\\_262364216](https://www.researchgate.net/figure/A-schematic-tokamak-figure-courtesy-of-C-Brandt_fig1_262364216) (visited on 10/20/2022).
- [15] Georg Friedrich Harrer. "On the origin and transport of small ELMs". PhD thesis. Technische Universität Wien, 2020. DOI: 10.34726/hss.2020.44863. URL: <https://doi.org/10.34726/hss.2020.44863>.
- [16] R. Fischer et al. "Integrated Data Analysis of Profile Diagnostics at ASDEX Upgrade". In: *Fusion Science and Technology* 58.2 (2010), pp. 675–684. DOI: 10.13182/FST10-110. eprint: <https://doi.org/10.13182/FST10-110>. URL: <https://doi.org/10.13182/FST10-110>.

- [17] K. Miyamoto. *Plasma Physics and Controlled Nuclear Fusion*. atomic, optical, and plasma physics. Springer Berlin Heidelberg New York, 2005. ISBN: 3-540-24217-1.
- [18] David Moiraf. *Poloidal cross section of the magnetic field of a tokamak*. 2021. URL: [https://www.researchgate.net/figure/Poloidal-cross-section-of-the-magnetic-field-of-a-tokamak-and-the-bean-shaped-part-of-the\\_fig2\\_354253660](https://www.researchgate.net/figure/Poloidal-cross-section-of-the-magnetic-field-of-a-tokamak-and-the-bean-shaped-part-of-the_fig2_354253660) (visited on 11/14/2023).
- [19] Lidija Radovanovic. *Ballooning stability analysis of the asdex-upgrade small-elm regime*. 2020.
- [20] Guillaume Brochard. *Trajectory of a trapped particles along the tokamak's magnetic field*. 2019. URL: [https://www.researchgate.net/figure/Trajectory-of-a-trapped-particles-along-the-tokamaks-magnetic-field-Its-dynamics-is\\_fig7\\_339686279](https://www.researchgate.net/figure/Trajectory-of-a-trapped-particles-along-the-tokamaks-magnetic-field-Its-dynamics-is_fig7_339686279) (visited on 12/05/2022).
- [21] A G Peeters. "The bootstrap current and its consequences". In: *Plasma Physics and Controlled Fusion* 42.12B (Dec. 2000), B231-B242. DOI: 10.1088/0741-3335/42/12b/318. URL: <https://doi.org/10.1088/0741-3335/42/12b/318>.
- [22] SP Hirshman. "Finite-aspect-ratio effects on the bootstrap current in tokamaks". In: *The Physics of fluids* 31.10 (1988), pp. 3150–3152.
- [23] O. Sauter, C. Angioni, and Y. R. Lin-Liu. "Neoclassical conductivity and bootstrap current formulas for general axisymmetric equilibria and arbitrary collisionality regime". In: *Physics of Plasmas* 6.7 (July 1999), pp. 2834–2839. DOI: 10.1063/1.873240. URL: <https://doi.org/10.1063/1.873240>.
- [24] E A Belli and J Candy. "Kinetic calculation of neoclassical transport including self-consistent electron and impurity dynamics". In: *Plasma Physics and Controlled Fusion* 50.9 (July 2008), p. 095010. DOI: 10.1088/0741-3335/50/9/095010. URL: <https://dx.doi.org/10.1088/0741-3335/50/9/095010>.
- [25] A. Redl et al. "A new set of analytical formulae for the computation of the bootstrap current and the neoclassical conductivity in tokamaks". In: *Physics of Plasmas* 28.2 (Feb. 2021), p. 022502. DOI: 10.1063/5.0012664. URL: <https://doi.org/10.1063/5.0012664>.

# Acknowledgements

Dear reader of this thesis!

After countless sleepless nights, I feel it is now the perfect moment to convey my profound gratitude. The successful completion of my bachelor's thesis signifies an extraordinary milestone in my undergraduate odyssey, affording me the singular chance to make a humble yet significant contribution to the realm of nuclear fusion research. I am brimming with profound pride and gratitude for this invaluable experience. While it is impossible to enumerate all the individuals who have inspired my pursuit of physics, I would like to acknowledge those who have played the most pivotal roles in guiding me along this journey.

## I wanna say thank you to:

- **Elisabeth Wolfrum** and **Friedrich Aumayr** for their exceptional guidance throughout the completion of this thesis. Their profound expertise in their respective fields is just amazing, and their ability to impart this knowledge in such an engaging manner is truly remarkable. If I were ever a contestant on a quiz show like the "Millionenshow," I would undoubtedly choose them as my telephone jokers without hesitation.
- **Lidija Radovanovic** for her unwavering support and patience. She went above and beyond by promptly responding to my late-night Discord messages and graciously explaining complex concepts, even when I needed the same information reiterated for the fifth time. Her belief in me and my thesis, even during moments when my own confidence waned, meant a lot to me.
- **Georg Harrer** and the entire Fusion team. It was an absolute delight to be a part of your group, and I am grateful for the valuable experiences and camaraderie I enjoyed during my time with you all.
- **Johanna Zach** writing her bachelor thesis with Lidija alongside me. It was incredibly comforting to discover that we were facing similar challenges in our research. Working alongside you has been not only effortless but also highly productive, as we supported and encouraged each other throughout this shared experience. I genuinely wish you all the best in your future endeavors.
- **Leopold Mechtler**, my high school teacher, who not only introduced me to the fascinating world of physics but also sparked a genuine interest in the subject within me. I will forever cherish this period as the inception of my passion for science and technology.
- my family **Theresa, Michael, Jonathan** and **Elias** for their unwavering support and assistance in every possible way. They've not only been there for me in times of need but also ensured I didn't go hungry, even when I was too engrossed to remember to eat.
- my grandparents **Gertraud, Karl, Johanna** and **Johann** for showing me that prioritizing the well-being of others over oneself is a fundamental aspect of being

a better human being. I wish each and every one of you could witness the accomplishments I've achieved thus far.

- my friends who have consistently supported me throughout my journey, even when it meant I couldn't join them for weeks when they gathered together. It's truly a blessing to have people you can always turn to during challenging times, individuals with whom you can share absolutely anything.
- the **Rasselbande**, the best group of people I could have ever hoped for when I entered university. You all have made my life so much better during the darkest days of struggle. While it saddens me that this chapter has come to an end, please know that I will always hold you close to my heart. I genuinely love each and every one of you. If my memory serves me right, we still have the Vienna Beer-Rally pending, don't we? ;-)

Lastly, I extend my heartfelt gratitude to you, the reader of this thesis. Science thrive on the trust that people place in them. I hold a firm conviction that technology represents the most promising avenue for addressing humanity's challenges and ensuring the well-being of every individual on this beautiful planet.

Samuel